### Title

Coupling of the mid-depth and abyssal components of the global overturning circulation according to a state estimate.




### Journal

Science Advances, 7(21)



### Authors

Rousselet, Louise

Cessi, Paola

Forget, Gael



### Publication Date

2021-05-01

### DOI

10.1126/sciadv.abf5478

Peer reviewed

CORRECTED 3 NOVEMBER 2021; SEE FULL TEXT

SCIENCE ADVANCES | RESEARCH ARTICLE

OCEANOGRAPHY

# Coupling of the mid-depth and abyssal components of the global overturning circulation according to a state estimate

**Louise Rousselet[1], Paola Cessi[1]*, Gael Forget[2]**



**Using velocities from a state estimate, Lagrangian analysis maps the global routes of North Atlantic Deep Water (NADW) exiting the Atlantic and reentering the upper branch of the Atlantic Meridional Overturning Circulation (AMOC). Virtual particle trajectories followed for 8100 years highlight an upper route (32%) and a lower route (68%). The latter samples $\sigma_2 > 37.07$ and is further divided into subpolar (20%) and abyssal cells (48%). Particles in the abyssal cell detour into the abyssal North Pacific before upwelling in the Southern Ocean. NADW preferentially upwells north of 33°S (67%). Total diapycnal transformations are largest in the lower route but of comparable magnitudes in the upper route, challenging its previous characterization as "adiabatic." Typical transit times are 300, 700, and 3600 years for the upper route, subpolar, and abyssal cells, respectively. The AMOC imports salinity into the Atlantic, indicating its potential instability to high-latitude freshwater perturbations.**

## INTRODUCTION

The meridional overturning circulation (MOC) of the ocean is a key component of Earth's climate system: It transports heat poleward in the Northern Hemisphere, generally reducing the equator-to-pole temperature difference there, but equatorward in the South Atlantic (*1*–*5*). The MOC includes northward flow of intermediate and upper waters from the Southern Ocean into the Atlantic, which are eventually transformed into North Atlantic Deep Water (NADW) in the Nordic Seas, Irminger Sea, Labrador Sea, and Iceland basins (*6*): This circulation forms the mid-depth overturning (red-shaded contours in the top panel of Fig. 1), which is confined to the Atlantic basin. An equivalent mid-depth overturning is absent in the Indian and Pacific sector (bottom panel of Fig. 1). Instead, there is an abyssal overturning, largely fed by the formation of Antarctic Bottom Water (AABW) around Antarctica and closed by diapycnal upwelling from deep to intermediate levels and by along-isopycnal return to the surface of the Southern Ocean (*7*) (blue-shaded contours below $\sigma_2$ = 37.07 in the bottom panel of Fig. 1). A schematic of the global overturning circulation and the nomenclature of its components are given in fig. S1 of the Supplementary Materials.

In the Southern Ocean, above 3000 m and poleward of 33°S, the continuation of the mid-depth overturning can be seen (red-shaded contours in both panels of Fig. 1), in addition to the subpolar cell (blue-shaded contours poleward of 50°S in both panels of Fig. 1). The subpolar cell in the Southern Ocean is confined to the southern half of the Antarctic Circumpolar Current (ACC) and is associated with the Weddell Sea gyre, which is emerging as an important player in the carbon budget of the Southern Ocean (*8*). The climatological meridional transport of the subpolar cell varies considerably among models of the Southern Ocean overturning, from 6 to 27 sverdrups (Sv) (*9*).

NADW downwelling in the high latitudes of the North Atlantic must be compensated by upwelling, which largely occurs outside the Atlantic basin (*10*, *11*). One return route is in the Southern Ocean, powered by wind-driven Ekman suction, whereby NADW is made lighter by buoyancy gain near the surface, returning directly to the upper limb of the MOC (*12*). After the transformations in the ACC region, most of the transport enters the Indo-Pacific and is further transformed within the subtropical gyres, before entering the Atlantic (*13*–*16*). This route has been considered to require minimal interior diapycnal processes, relying primarily on transformations in the surface diabatic layer (*16*–*18*). According to this view, NADW gets transformed directly into lighter water, without undergoing substantial densification in the abyssal ocean. We call this pathway the "upper route," because the transformations occur primarily in the upper ocean.

Alternatively, NADW can first be recycled to lower buoyancy classes, identified as AABW, and subsequently upwelled diffusively over the global ocean (*7*, *10*, *19*). Interior diapycnal upwelling can occur anywhere, but it is thought to be particularly effective in the abyssal region, where mixing is enhanced (*20*, *21*), and in the Pacific, because of its large extent. We call this pathway the "lower route."

The distinction between the two routes is important because the lower route has longer residence time scales and thus contributes differently from the upper route to the ventilation of the ocean interior and the potential sequestration of surface properties such as heat and carbon (*22*). For example, one hypothesis is that, during the Last Glacial Maximum (LGM), the larger extent of Antarctic ice induced a more vigorous abyssal overturning than in the modern climate, at the expense of a reduced mid-depth cell, leading to more effective oceanic sequestration of carbon (*23*, *24*). Additional carbon sequestration would have been provided by a reduced connection between the mid-depth and abyssal cells during the LGM (*25*). The lower route couples the mid-depth and abyssal components of the global overturning circulation. However, the partition between the upper and lower routes in nature is not agreed upon even for the modern climate: The most recent estimates using hydrographic observations attribute between 75% (*7*) and 100% (*19*) to the lower route.

The combination of the mid-depth and abyssal overturns forms the global overturning circulation. The zonally integrated view of Fig. 1 hides the connections between these two overturns and between different longitudinal sectors of the ocean. A major difficulty with identifying routes for the return of NADW to the upper branch of

[1]Scripps Institution of Oceanography, University of California, San Diego, La Jolla, CA 92093, USA. [2]Department of Earth, Atmospheric and Planetary Sciences, Massachusetts Institute of Technology, Cambridge, MA 02139, USA.
*Corresponding author. Email: pcessi@ucsd.edu

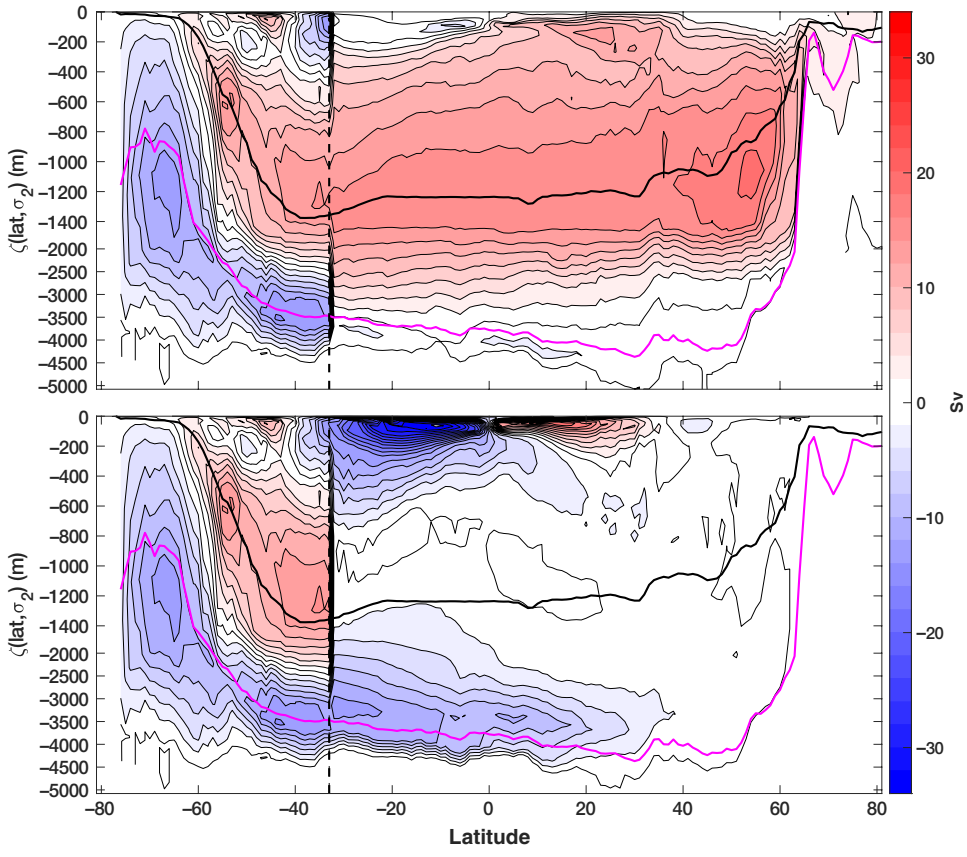


**Fig. 1. Residual MOC vertically integrated above surfaces of constant $\sigma_2$ as a function of latitude (abscissa) and $\sigma_2$ (ordinate), time-averaged, and zonally integrated.** The zonal integration is over all longitudes south of 33°S (black dashed line) but only in the Atlantic sector (**Top**) and in the Indo-Pacific sector (**Bottom**) north of 33°S. The density ordinate is remapped into a depth-like coordinate ζ(latitude, $\sigma_2$) defined as the time- and zonally averaged (over all longitudes) depth of each $\sigma_2$ surface. The ECCO4 (release 3) horizontal velocity (Eulerian + bolus), temperature, and salinity fields are used. Positive (negative) values in red (blue) shading indicate clockwise (anticlockwise) circulation. The contour interval is 2 Sv (1 Sv = $10^6$ $m^3/s$). The thick black line marks the depth ζ(latitude, $\sigma_2$ = 36.6 $kg/m^3$), which approximately divides the upper and lower branches of the residual MOC. The thick magenta line marks the depth ζ(latitude, $\sigma_2$ = 37.07), which approximately bounds the lower branch of the residual mid-depth cell from below.

the MOC is that interbasin connection is mediated by zonal currents in the Southern Ocean and is dominated by the powerful ACC. The ACC has a vertically integrated zonal transport of about 150 Sv (1 Sv = $10^6$ $m^3/s$), while the MOC carries only about 14 Sv into and out of the Atlantic, i.e., the MOC is a small fraction of the zonal transport in the Southern Ocean (*26*).

Lagrangian analysis is an effective methodology to quantify the pathways of the MOC, while overcoming some difficulties of Eulerian analysis. It also allows quantification of the salinity export by the MOC along its path. According to simple models, the salinity export out of the Atlantic by the MOC is an indicator of the stability of the MOC (*27*–*30*). The Atlantic receives more evaporation than precipitation, and thus, salinity is exported out of the basin, when all the components of the velocity are considered. However, if the velocity associated with the MOC imports salinity into the Atlantic, then the salt-advection feedback operates, and it can destabilize the MOC, given suitable high-latitude freshwater perturbations (*31*). Realistic coupled ocean-atmosphere models with eddy-permitting ocean resolutions confirm that the MOC imports salinity into the Atlantic and that it can be destabilized (*32*). Because this stability criterion is based on the freshwater (or salinity) transport by the MOC only and not on the freshwater (or salinity) transport by all velocity components, it is difficult to estimate it from Eulerian measurements. An approximation of the MOC salinity transport based on Eulerian observations finds that the MOC exports fresh water out of the Atlantic, indicating the possibility of destabilization (*33*). The Lagrangian method is a complementary approach, which provides a useful check on the accuracy of the Eulerian approximation.

In this study, we estimate the partition of the lower versus the upper routes for the return of NADW to the upper branch of the Atlantic MOC (AMOC) using a Lagrangian methodology. Multimillennia statistics of virtual particle trajectories using data-constrained velocities quantify the coupling between the mid-depth and abyssal overturning components of the global overturning circulation. Typical transit times, diapycnal transformation, and salinity transport along these routes are measured.

## METHODS

The method consists of tracking particle trajectories backward in time from an "exit" section in the South Atlantic (here, 6°S above a target density surface) to specific "entry" sections. The quantification

of mass transport with particle trajectories is performed by initially seeding the exit section with a large number of particles whose concentration is proportional to the local transport. Each particle is weighted in proportion to the volume transport, divided by the number of particles, at the initial grid cell. The initially assigned transport weight is then conserved following the trajectory because the velocity vector field conserves mass (volume). This type of calculation has been successfully performed using velocity fields from ocean general circulation models (*34*–*36*) and with the velocity from a global state estimate (*37*).

To estimate Lagrangian transport, incompressible velocities over a global grid are required. An observational estimate that satisfies these requirements is the three-dimensional, time-variable, incompressible velocity from "Estimating the Circulation and Climate of the Ocean" (ECCOv4) (*38*, *39*). These velocities, together with temperature and salinity, are a dynamically consistent assimilation of more than 1 billion oceanographic observations between 1992 and 2015 into a dynamically consistent model. Figure 1 shows the time-averaged and longitudinally integrated MOC from ECCOv4 calculated in density coordinates and latitude, using $\sigma_2$, i.e., potential density referred to 2000 dbar, as the vertical coordinate [more details on the velocity fields can be found in (*37*) and in the Supplementary Materials].

## The ECCO estimate

As in (*37*), the velocities used in the calculation of Lagrangian trajectories are the monthly climatologies available in the release 3 of ECCOv4 on the native model grid at 1° horizontal resolution [the Lat-Lon-Cap-90 grid as defined in (*38*)] and with 50 vertical levels (*38*, *39*). These velocities are derived from the dynamically consistent assimilation of more than 1 billion observations for the period 1992 to 2015 into a primitive-equation ocean–sea ice model that satisfies exact conservation laws for mass, momentum, temperature, salinity, and sea ice.

The assimilated data consist of satellite products (along-track altimetry, mean dynamic topography, remotely sensed ocean bottom pressure, sea surface temperature, sea ice concentration, and surface salinity) and temperature and salinity profiles collected in situ (including from all Argo floats). To minimize misfit between the model and the observations, several model parameters are optimized (*38*, *39*): initial conditions in January 1992, air-sea interactions throughout 1992 to 2015, and parametrized turbulent transports (*38*, *40*–*42*).

Many studies have looked at various metrics to evaluate the ECCOv4 estimate, which collectively affirm its value for understanding both the ocean climatology and its variability from observations (*38*, *39*, *43*, *44*). The estimate of the MOC according to ECCOv4 is in broad agreement with several independent (i.e., not assimilated) estimates [see Table 1 in (*26*)]. The ACC transport at Drake Passage in ECCOv4 is 150 Sv, which is intermediate between the two recent independent "in situ" estimates in (*45*) (134 ± 11 Sv) and (*46*) (173 ± 11 Sv) and in the middle of the ensemble of estimates compiled in (*47*) (152 ± 19.2 Sv). In the state estimate used in this study, the Southern Ocean subpolar cell carries 13.5 Sv, an amount intermediate among those in (*9*) (6 to 27 Sv). In addition, the zonally integrated abyssal overturning carries 14.4 Sv, an estimate close to the Southern Ocean state estimate of 13 ± 6 Sv (*48*) but smaller than the two recent hydrography estimates of 20.9 ± 6.7 Sv (*7*) and 26.9 ± 7.6 Sv (*49*).

An important consideration in our choice of this state estimate is that the parametrized advective fluxes of mesoscale eddies and the isopycnal and diapycnal tracer diffusion rates were optimized to minimize model-data misfit in ECCOv4 (*38*, *42*). Not only does this optimization of sub-grid scale transport terms play a leading role in achieving a close fit to data over 1992 to 2015, but it also greatly reduces spurious model drifts over multicentennial time scales (*42*). Hence, ECCOv4's gridded transport estimate can be viewed as an inversion, which produces a realistic long-term mean ocean state. This feature of ECCOv4 makes it particularly suited to the study of long time scales in the global ocean circulation.

One measure of the MOC is the "residual" transport within isopycnal layers rather than depth layers. The residual overturning circulation measures the (potential) density transport rather than the volume transport: It is more meaningfully associated with the transport of buoyancy than the overturning in depth coordinates (*50*), because it captures the transport not only by the average meridional velocity but also by waves, eddies, and gyres with zero time- or zonally averaged velocity. Transport of tracers other than buoyancy is subject to additional along-isopycnal diffusion, which is not included in the residual overturning calculation.

Because ECCOv4 does not resolve mesoscale processes, the eddy flux of tracers is parametrized in terms of isopycnal diffusion and a "bolus" velocity related to the slope of isopycnals (*40*, *41*, *51*). Thus, in ECCOv4, the appropriate way to calculate the residual transport of the MOC is to use the sum of Eulerian velocity plus the bolus velocity, integrated over density layers rather than depth layers, as shown in Fig. 1. Accordingly, as in (*37*), the velocity used to calculate Lagrangian trajectories is the sum of Eulerian velocity plus the bolus velocity in all three dimensions.

## Calculation of Lagrangian trajectories

Because the ECCOv4 state variables are on a fairly coarse grid, about 1° each in latitude and longitude, we can use monthly mean velocities, seeding a sufficient number of particles for each month for 12 months only. There is little difference in Lagrangian statistics when using more frequently sampled velocities at this resolution (*52*). Thus, we can use a moderate number of particles, integrating trajectories for 8100 years, which is the required time to recover almost 90% of the particles. This long time scale is associated with the slow transit in the abyssal cell. This length of integration would not be feasible with a velocity field at eddy-permitting resolutions, where velocity averages need to be five daily at most, requiring more frequent initial particle seeding, and a total number of particles at least six times larger than with monthly averaged velocities (*53*).

To determine Lagrangian trajectories, the ECCOv4 climatological monthly velocities are linearly interpolated in space using an incompressibility-preserving, transport-weighted algorithm (*34*, *54*) and linearly interpolated in time to obtain a 1-year periodic time series. Because the climatological monthly volume transports are 1-year periodic, the annual cycle can be repeated as many times as needed, without introducing discontinuities that artificially alter the trajectories: This three-dimensional field is used to advect virtual particles backward in time for 8100 years (more details in the Supplementary Materials). Allowing interannual variability of the monthly averages would require the initial monthly seeding to be repeated for all 24 years of the record, requiring an unmanageable number of particles.

In practice, a total of 63,482 particles are seeded at 6°S in the South Atlantic, at depths above the $\sigma_2$ = 36.6 kg/m$^3$ surface: This defines the "exit section," which carries 13.6 Sv northward. The $\sigma_2$ = 36.6 kg/ m$^3$

surface marks the lower boundary of the upper, northward branch of the MOC (cf. the black thick lines in the top panel of Fig. 1). Each particle is weighted by about $(2 \pm 0.15) \times 10^{-4}$ Sv so that the number of particles per each grid face on the section is proportional to the transport of that grid face (the exact weight of each particle is recorded). Because the three-dimensional velocity vector is exactly incompressible, the transport weight of each particle is conserved following the trajectory (*34*, *54*). Conservation of transport is used to quantify the mass flux through different sections, determining the routes taken by NADW to rejoin the upper branch of the MOC. The temperature and salinity along the trajectories are also recorded.

Particles are then tracked backward in time until they cross again the section at 6°S flowing northward, which identifies the NADW flow at 6°S. The NADW section at 6°S is the entry section, whereas the initial section at 6°S ($\sigma_2 \leq 36.6$ kg/m$^3$) is the exit section, defining the return upper limb of the AMOC into the North Atlantic. To characterize the entry section of NADW, these additional constraints are prescribed: Particles have to exit the South Atlantic and Indian sector through either the Drake Passage (66°W, DP hereafter), the Indonesian Throughflow (116°E, IT hereafter), or Tasman Leakage (130°E, TL hereafter), or they can cross back directly 6°S in the Atlantic sector but for $\sigma_2 > 36.6$ kg/m$^3$. These sections are marked in Fig. 2 and labeled in Fig. 3: They are the locations of constraints for the global overturning circulation pathways into and out of the South Atlantic. These constraints exclude recirculations within the upper limb of the mid-depth MOC, such as the shallow subtropical Ekman cells, which we do not associate with the mid-depth overturning. The routes of NADW are determined by recording the place and time of the first passage from the entry section to the exit section at 6°S. Hereafter, we describe particle trajectories as forward in time. To highlight the different routes taken by NADW, we divide the trajectories into three groups as follows:

1) The upper route is defined as the trajectories going from the NADW entry section to the exit section, without crossing the $\sigma_2 = 37.07$ kg/m$^3$ surface (group 1). This group quantifies the portion of NADW that does not circulate in the range of abyssal densities, rejoining the upper limb of the MOC directly. Particles in this route undergo transformations of NADW directly into less dense waters. This route carries 4.4 Sv (32% of the total transport).

2) The lower route is defined as the trajectories going from the entry section to the exit section, after crossing the $\sigma_2 = 37.07$ kg/ m$^3$ surface. It amounts to 7.6 Sv. This route is further divided into two groups:

2a) We define the subpolar cell as the group of trajectories crossing the $\sigma_2 = 37.07$ kg/ m$^3$ surface only south of 30°S (group 2). This group quantifies the portion of NADW that circulates in the range of abyssal densities but confined to the subpolar region of the Southern Ocean, without sampling the abyssal Indian or Pacific basins. The portion of NADW identified by this group is transformed into denser water south of 30°S, before rejoining the upper limb of the AMOC. It amounts to 2.7 Sv (20% of the total transport).

2b) We define the abyssal cell as the group of trajectories crossing the $\sigma_2 = 37.07$ kg/ m$^3$ surface both south and north of 30°S (group 3). This group quantifies the portion of NADW that recirculates in the range of abyssal densities sampling the abyssal Indian and/or Pacific basins, i.e., NADW becomes denser before rejoining the upper limb of the AMOC. This is the main component of the lower route, amounting to 4.9 Sv (36% of the total transport).

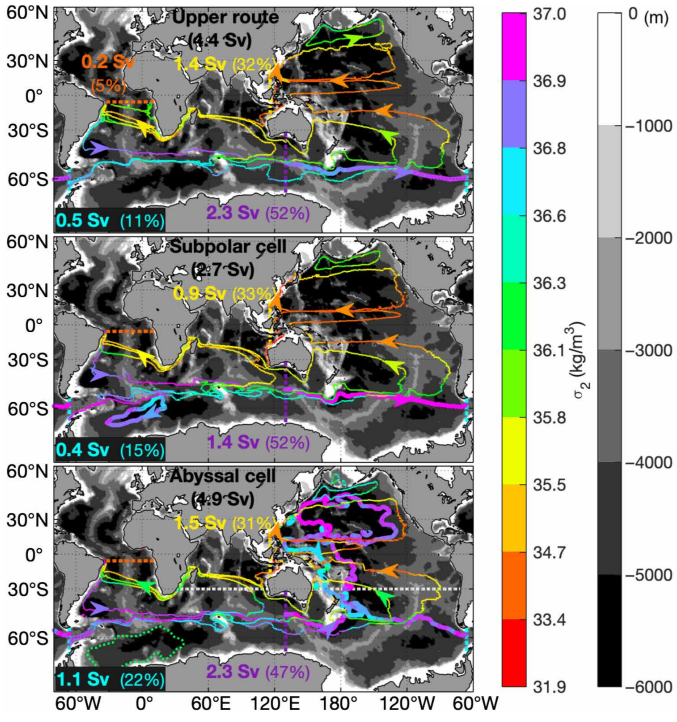


**Fig. 2. Position of the median Lagrangian transport streamfunctions between section pairs (contours).** The value of $\sigma_2$ (kilograms per cubic meter) in 1° × 1° bins at the median streamline position, transport-weighted and particle-averaged over the vertical column, is shown in color shading. (**Top**) Reconstruction for trajectories in the upper route, i.e., that never cross $\sigma_2 = 37.07$ kg/m$^3$ between the entry and exit sections at 6°S. (**Middle**) Reconstruction for trajectories in the subpolar cell, i.e., crossing $\sigma_2 = 37.07$ kg/m$^3$ only south of 30°S between the entry and exit sections at 6°S. (**Bottom**) Reconstruction for trajectories in the abyssal cell, i.e., crossing $\sigma_2 = 37.07$ kg/m$^3$ both south and north of 30°S between the entry and exit sections at 6°S. In the bottom panel, the 10% contour of the Lagrangian streamfunction in the Weddell Sea is also shown. The section pairs used are listed at the beginning of the "Lagrangian reconstruction" section in the Supplementary Materials. Bathymetry is shown in grayscale background. The color-coded numbers show the transport across the nearest section and their percentages.

A final group of trajectories going from the entry section to the exit section, after crossing the $\sigma_2 = 37.07$ kg/ m$^3$ surface only north of 30°S, is almost empty (222 particles) and thus not considered hereafter.

The computation was repeated for the first 512 years with double the number of particles, and the transport values at a target section differ at most by 0.2% over that time from those with 63,482 particles (*37*). Thus, the multimillenial integration was confidently performed with 63,482 particles. By the end of the 8100-year integration, about 4.5% of the particles get stuck on topography (coasts or seafloor). To close the transport budget, the individual transport carried by the stuck particles is redistributed among the particles initially launched in the same grid cell (more details in the Supplementary Materials).

Notice that the sum of the transports of the three groups enumerated above amounts to 12 Sv, which is 88% of the 13.6 Sv of the exit section. This is because, after 8100 years, 1.6 Sv have not yet reached (backward in time) the common entry section, i.e., 12% of the NADW has not yet entered the upper branch of the AMOC. However, as detailed in the "Transit times of the global overturning circulation"

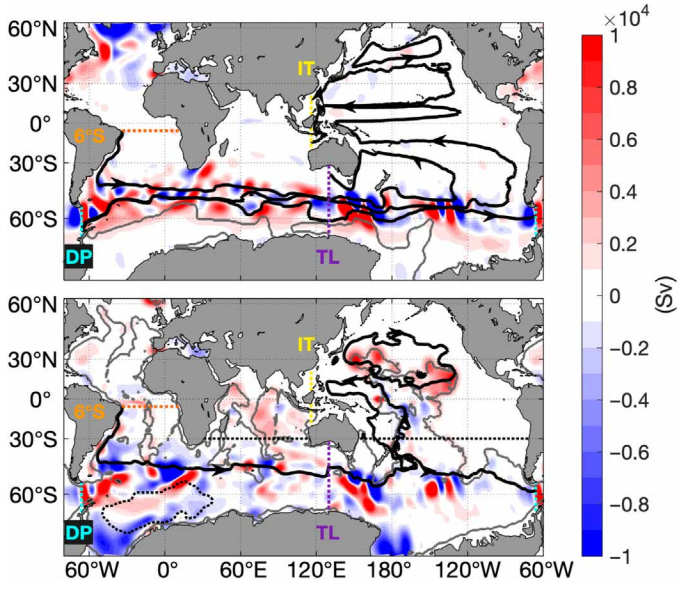


**Fig. 3. Annual climatologies of diapycnal velocity across selected isopycnals.** (**Top**) Diapycnal velocity across the isopycnal $\sigma_2$ = 36.6 kg/m$^3$, positive upward (color shading), and isopycnal outcrop's position (intersection with sea surface, gray contour). (**Bottom**) Diapycnal velocity across the isopycnal $\sigma_2$ = 37.07 kg/m$^3$ (color shading) and isopycnal incrop position (intersection with bathymetry, gray contour). The diapycnal velocity field is smoothed over three grid points in both horizontal directions. A subset of the median streamlines of the upper route in the top panel and for the abyssal cell in the bottom panel are drawn in black contours (solid and dashed) (cf. Fig. 2, top and bottom). The color-coded lines mark the position of sections 6°S, TL, IT, and DP.

section, we can confidently attribute these 1.6 Sv to the sluggish abyssal cell that contains the slowest group of trajectories, with transit times longer than 8100 years.

## RESULTS

### Reconstruction of the NADW routes to the upper limb of the AMOC

An objective reconstruction of the main pathways of the AMOC is obtained by computing the horizontal streamfunction (in 1° × 1° bins) associated with the vertical sum and cumulative zonal sum of each particle meridional transport (magnitude and sign). We compute successive streamfunction segments considering only the first passage (backward in time) between several section pairs (*55*). The methodology is detailed in the Supplementary Materials.

The typical path of particles in each group is illustrated by the streamfunction contour with the median transport value on that segment (hereafter referred as the median streamlines). We also estimate density along the trajectories by computing the transport-weighted vertical ensemble average of the particles $\sigma_2$ at the latitude and longitude of the median streamlines (Fig. 2). An analogous estimate of depth along the median streamlines is given in fig. S2 of the Supplementary Materials.

Figure 2 shows the reconstruction of the routes (colored contours) for each group. The contours are the median streamlines, and the color of the contours displays $\sigma_2$. Although all individual trajectories go from the entry to the exit sections, the median streamline representation shows some closed contours (e.g., the North Pacific subpolar gyre). Thus, the reconstruction, while representative of particle trajectories, is not an actual trajectory. Representative examples of particle trajectories are given in the animation of the Supplementary Materials. In addition, distribution maps (number of particles in grid cells) are also shown in the Supplementary Materials. The animations and distribution maps illustrate the complexity of particle paths.

Figure 2 is divided into three panels, one for each group. All three reconstructions share some common features that are shown as thin contours. Specific characteristics for each group are highlighted by thick contours.

The top panels of Fig. 2 and fig. S2 refer to particles in the upper route. From 6°S, NADW flows southward on the western boundary of the South Atlantic and then densifies (deepens) while flowing eastward along the northern edge of the ACC (purple contour). The initial densification (deepening) of trajectories exiting the South Atlantic is associated with the diapycnal downwelling across $\sigma_2$ = 36.6 kg/m$^3$ that prevails in the northern portion of the ACC, as shown in Fig. 3 (top; details on the calculation of the diapycnal velocity are given in the Supplementary Materials). Subsequently, particles circulate multiple times around Antarctica in a southward and upward spiral as described in (*56*) (trajectories not displayed). The last paths before abandoning the circumpolar region (cyan contours) are further south and less dense (shallower) than the first circumpolar path (purple contours). From the ACC, particles go either in the subtropical gyre of the Indian Ocean (yellow contours) or sample the gyres of the Pacific, before exiting through either TL or IT. Ninety-seven percent of all trajectories go through the Agulhas leakage, where they all reach the same density range (34.7 to 35.5 kg/m$^3$), crossing the Atlantic westward to the east coast of Brazil (*37*). Of the 4.4 Sv flowing in the upper route, 11% go through the South Indian Ocean only (0.5 Sv), while 52 and 32% go around the South (2.3 Sv) and North (1.4 Sv) Pacific, respectively. A small fraction (5% or 0.2 Sv) crosses 6°S below $\sigma_2$ = 36.6 kg/m$^3$ going southward, taking a shortcut into the upper limb of the AMOC in the tropical region of the South Atlantic.

Trajectories in the subpolar cell (Fig. 2 and fig. S2, middle) originate from the intermediate-density portion of the NADW branch of the AMOC, i.e., denser (deeper) than in the upper route. When NADW leaves the western boundary current in the Atlantic basin (around 35°S), particles take a more northerly and denser path than those in the upper route (purple/magenta contours). This more northerly path in the South Atlantic is between the two paths described in (*57*). The densification (deepening) of trajectories exiting the South Atlantic is associated with the diapycnal downwelling across $\sigma_2$ = 37.07 kg/m$^3$ that prevails in the northern portion of the ACC, as shown in Fig. 3 (bottom). During the multiple circuits around the ACC, 63% of the transport recirculates clockwise in the Weddell Sea gyre (closed contours centered at 0°E and 70°S), a feature absent in the upper route (Fig. 2, top). A small fraction recirculates clockwise in the Ross Sea gyre (7%). The upwelling (downwelling) on the north (south) side of the Weddell Sea gyre in Fig. 3 is associated with the upward (downward) branch of the anticlockwise meridional cell poleward of 55°S visible in both panels of Fig. 1. After the circumpolar paths in the southern part of the ACC, the subpolar cell group follows a similar fate to the upper route. Although dense, the subpolar cell paths never reach abyssal depths: In depth space, the subpolar cell is closer to the upper route than to the abyssal cell (cf. fig. S2). The 2.7 Sv reaching 6°S in this group all converge into

the Agulhas leakage through the following routes: 0.4 Sv (15%) go around the South Indian Ocean only, and 1.4 Sv (52%) and 0.9 Sv (33%) go around the South and North Pacific Ocean, respectively.

The pathways for trajectories in the abyssal cell originate from the densest (deepest) portion of the NADW branch of the AMOC (Fig. 2 and fig. S2, bottom). Similarly to the other pathways, the median streamline densifies (deepens) while following the northern edge of the ACC until about 170°E. Because abyssal trajectories are strongly steered by bathymetry, and the ACC zonal flow is weak below 2500 m, they turn northward into the Pacific basin at Campbell Plateau–Chatham Rise, just east of New Zealand, forming the deep western boundary current of the South Pacific (*58*). From there, they continue along the Kermadec Ridge to eventually reach the subtropical North Pacific (*59*). This is the only group of particles that, on average, first takes a deep tour into the North Pacific before circulating around the ACC (only 9% of the abyssal cell transport first travels into the ACC before entering the North Pacific). The abyssal North Pacific is sampled with a clockwise and upward motion (magenta contours) following the bottom sloping boundaries of the basin marked by the position of the $\sigma_2$ = 37.07 kg/m$^3$ incrop (gray contours in the bottom panel of Fig. 3) in agreement with several modeling studies (*60*–*63*). The maxima of upwelling across this isopycnal surface correspond to the ascending branch of the abyssal overturning located between the equator and 30°N (cf. blue-shaded contours in the bottom panel of Fig. 1). The median streamline then enters the ACC at about 40°S and starts the circumpolar spiraling trajectories in the ACC common to all groups. In this group, a small fraction (8%) travels in the Ross Sea gyre, while 16% of the trajectories sample the Weddell Sea gyre (dashed blue contours showing 10% of the Lagrangian transport streamfunction), i.e., a substantially smaller fraction than in the subpolar cell. The final partition before joining the upper cell of the AMOC is as follows: 22% (or 1.1 Sv) go around the South Indian Ocean only, 47% (or 2.3 Sv) go around the South Pacific Ocean, and 31% (or 1.5 Sv) go through the North Pacific and across the IT.

The Lagrangian reconstruction of Fig. 2 and fig. S2, based on the first-passage median streamline, gives the impression of laminar, coherent trajectories. In reality, the global overturning circulation is a heterogeneous aggregate of many different pathways. A complementary view is obtained with the distribution map of the particle positions for all particles at all times and depths, binned in 1° × 1° latitude-longitude areas (fig. S3). This diagnostic captures the complexity of the paths, especially in the abyssal Pacific and Indian Ocean (fig. S3, bottom), tied to topographic steering. In addition, the multiple circumpolar loops are revealed, while they are purposefully removed in the Lagrangian reconstruction. As with the Lagrangian reconstruction, the particle distribution map shows a close similarity between the subpolar cell and the upper route trajectories, except that the upper route does not sample the subpolar side of the ACC, because of the constraint that $\sigma_2 < 37.07$.

In summary, the returns to the upper limb of the AMOC in the upper route and subpolar cell undergo both densification and upwelling in the ACC: NADW directly rises in the Southern Ocean, in a southward and upward spiraling motion within the ACC, before returning to the North Atlantic in upper layers either through the Indian, the South, or the North Pacific oceans (*19*, *56*). We find that 32% of NADW does not go through any abyssal pathway, in quantitative agreement with the estimate in (*7*) but in disagreement with (*19*), which attributes 100% to the lower route. Furthermore, we find that the lower route is divided into two separate groups: the subpolar cell and the abyssal cell. The confinement of the subpolar cell to the subpolar gyres of the Southern Ocean, especially the Weddell Sea gyre, without sampling the abyssal Indo-Pacific has not been illustrated before. In addition, the abyssal cell, which carries 70% of the lower route, first gets densified in the Indo-Pacific and then flows directly into the abyssal North Pacific, where it upwells before sampling the southern edge of the ACC. This pattern differs from the schematic proposed in (*19*) where abyssal water formation occurs at the Antarctic margin after upwelling in the ACC. The steady-state Eulerian view confounds the pathways of the subpolar and abyssal cells, giving the impression that densification near Antarctica is necessary for circulation in the abyssal North Pacific. However, these two pathways are well separated in their density change and transit time distributions, as shown in the next two sections.

## Diapycnal transformations in the global overturning circulation

The Lagrangian analysis provides a detailed view of the thermodynamical transformations occurring along the particle trajectories. In addition, maps of the change in $\sigma_2$ along the trajectory, $d\sigma_2$, complete the geographical distribution of diapycnal transformations for all three groups (fig. S4 in the Supplementary Materials). The precise definition of $d\sigma_2$ is given in eq. S10 of the Supplementary Materials. Some features common to all three groups are as follows (cf. Fig. 2 and fig. S4):

1) Densification at the northernmost edge of the ACC (~40°S);
2) Buoyancy gain in the central part of the ACC (~58°S);
3) Buoyancy gain in the equatorial Indo-Pacific basin;
4) Buoyancy gain in the eastern Pacific;
5) Densification in the subtropical regions of the Pacific and Indian Oceans, especially in regions of boundary currents;
6) Densification along the Antarctic margin, especially in the Weddell and Ross Seas for the subpolar and abyssal cells.

The Lagrangian analysis can distinguish the buoyancy gain (i.e., diapcynal upwelling) in the Southern Ocean versus the remaining basin regions. We find that, south of 33°S, only 31% of the upper route, 48% of the subpolar cell, and 26% of the abyssal cell first upwell through $\sigma_2$ = 36.6 kg/m$^3$ (similar numbers are obtained using 30°S instead of 33°S): The Southern Ocean and the ACC are not the most important sites for NADW upwelling as previously attributed (*16*–*18*). Examples of the detailed locations of transformation for typical particle trajectories can be found in the animation included in the Supplementary Materials.

A complementary quantification of the transformations along the different routes is presented in Fig. 4, which shows the two-dimensional, normalized distribution of $d\sigma_2$ in the three groups of particles as a function of density class (*64*) and sign, $P^{\pm}$. The precise definitions of $P^{\pm}$ are given in the Supplementary Materials (eq. S11). Positive and negative $d\sigma_2$ values are kept separate, and their absolute value is plotted on a logarithmic scale. All three distributions are skewed toward negative $d\sigma_2$ values, as appropriate for the overall buoyancy gain associated with NADW transformations into upper and intermediate water (Fig. 4). In the upper route and subpolar cell groups, transformations are centered around $\sigma_2 \approx 36.6$ kg/m$^3$, which is the isopycnal dividing the upper and lower limbs of the MOC. In the abyssal cell, transformations are maximum around $\sigma_2 \approx 37.07$ kg/m$^3$, which is the lower boundary of the mid-depth overturning in the Atlantic.

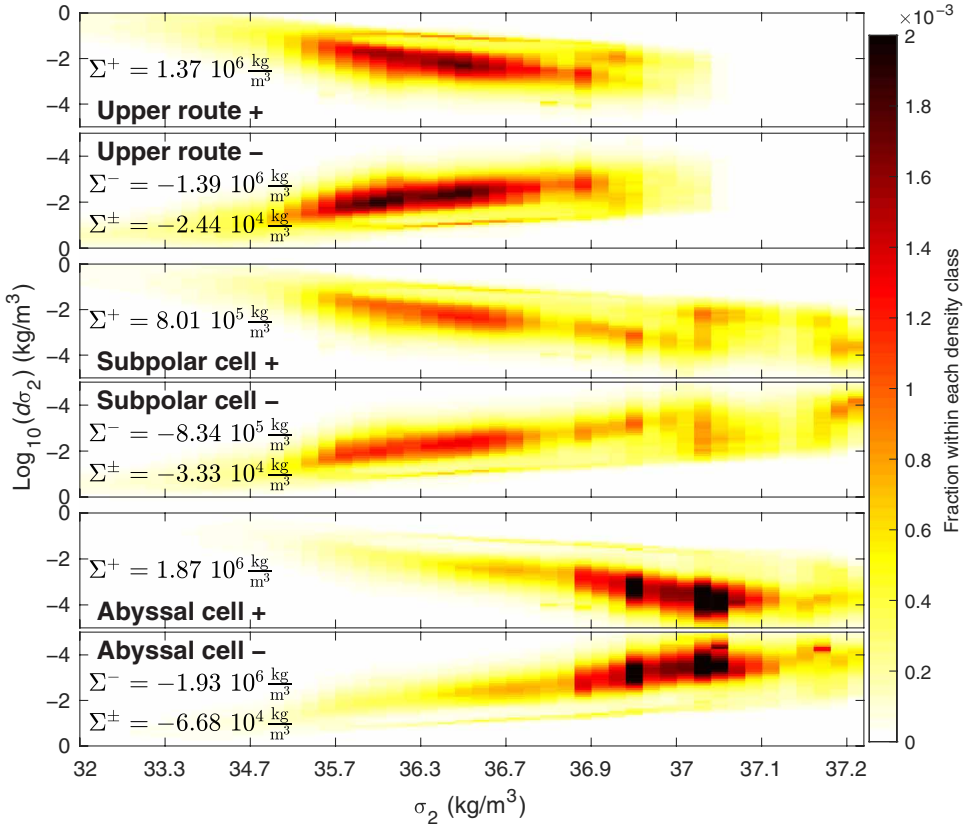


**Fig. 4. Distributions of $d\sigma_2$ for particles on each trajectory 2 months apart, segregated by $\sigma_2$ classes.** Upper route (top two panels), subpolar cell (middle two panels), and abyssal cell (bottom two panels). The bin size for $d\sigma_2$ is $5 \times 10^{-5}$kg/m$^3$, while the bin size for $\sigma_2$ decreases for increasing $\sigma_2$ values to account for the decrease in stratification. The sums over the bins with $d\sigma_2$ positive, $\Sigma^+$, negative, $\Sigma^-$, and the total $\Sigma^\pm \equiv \Sigma^+ + \Sigma^-$ are recorded. The distributions are normalized by the total number of particles present at all times in the respective group.

The total diapcynal transformations, summed over all density classes and all $d\sigma_2$, can be written as (we keep positive and negative separate)

$$\Sigma^+ \equiv \sum_{d\sigma_2>0,\sigma_2} \Delta_n P^+(d\sigma_{2n}, \sigma_2) \quad (1)$$

where the sum is taken over the number of particle in each group, and $\Delta_n$ is the bin size in $d\sigma_{2n}$ space. An analogous definition, denoted by $\Sigma^-$, is used for the sum over negative values of $d\sigma_2$. $\Sigma^+$, $\Sigma^-$, and their sum, $\Sigma^\pm$, are reported in Fig. 4. $\Sigma^\pm$ measures the total diapycnal change encountered along the Lagrangian trajectories for each group. The diapcynal transformation diagnostic (Fig. 4) confirms that buoyancy gain dominates for all groups, and the net buoyancy gain is largest for the abyssal cell and smallest for the upper route. At the same time, the upper route undergoes ample transformations, of similar magnitude and at similar locations as the abyssal cell. Therefore, it is not appropriate to characterize the upper route as an "adiabatic route" as it is often done (*16*–*18*).

## Transit times of the global overturning circulation

The transit times of the three groups quantify the time scales of the different pathways and their diapycnal changes. Figure 5 shows the distributions of transit times for the three groups of particles, weighted by transport. The top panel is for the upper route: The median transit time at 331 years and the 90th percentile at 1368 years are well captured by the 8100-year-long computation. The middle panel is for the subpolar cell: The median transit time (677 years) and 90th percentile (2051 years) are longer than those of the upper route, a consequence of the denser pathways taken in the subpolar cell. For both the upper route and subpolar cell, the last 1000 years (between 7100 and 8100 years) carry only 0.001 and 0.002 Sv, respectively. These small values indicate that after 8100 years, we have recovered more than 99% of the upper route and subpolar cell total transport.

The longest route is the abyssal cell (bottom): The median transit time at 2805 years and the 90th percentile at 5279 years are not captured by the 8100-year-long computation. Transit times between 7100 and 8100 years, shown as blue bars in Fig. 5, account for 0.1 Sv of the 4.9 Sv carried by the abyssal cell. Because the distribution of this group has not decayed sufficiently after 8100 years, the remaining 1.6 Sv of slow trajectories, which still have not crossed 6°S in the NADW range (backward in time), belongs to this group. Taking into account the total 6.5-Sv transport belonging to this group, the median time is 3597 years.

In summary, the transit times for the overturning in the subpolar cell are about twice as long as those in the upper route because of the denser (deeper) paths of the subpolar cell. However, both distributions are quite similar and share the same peak at around 200 years. The typical transit times in the abyssal cell are one order of magnitude larger than in both the upper route and the subpolar cell.

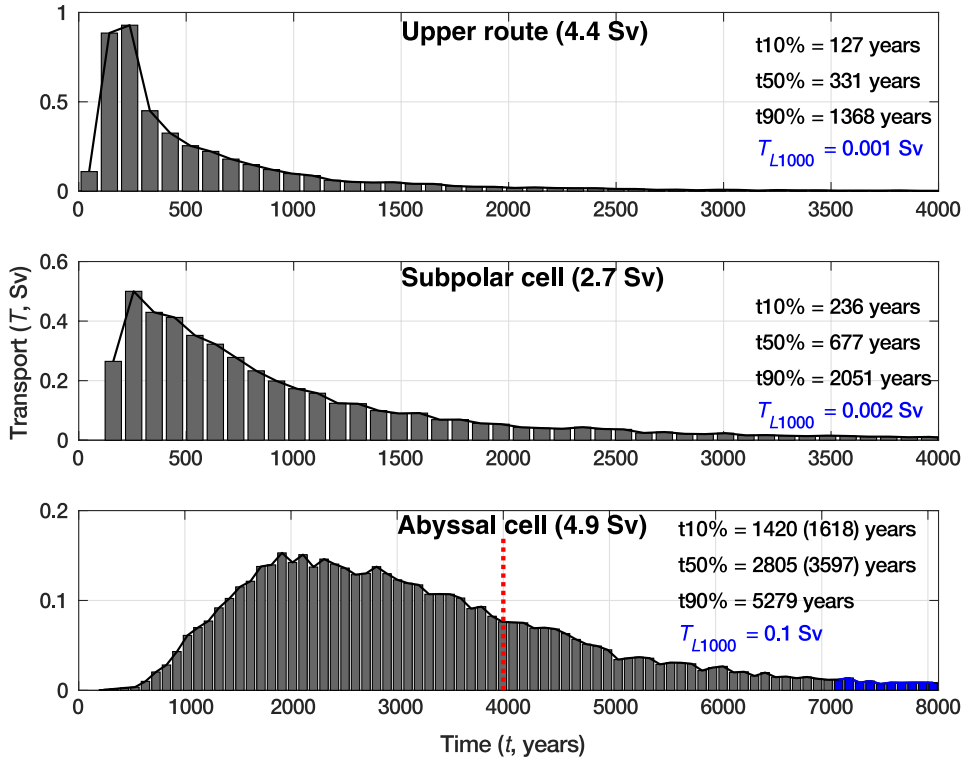


**Fig. 5. Transport-weighted distribution of transit times from the entry to the exit sections weighted by transport, in 100-year bins.** Please note the different *x*-axis limits in the top and middle panels compared to the bottom panel. The inset records the 10th percentile (t10%), median (t50%), and the 90th percentile (t90%) transit times and the fraction of transport for the transit times between 7100 and 8100 years ($T_{L1000}$). (**Top**) Upper route. (**Middle**) Subpolar cell. (**Bottom**) Abyssal cell. In the bottom panel, the 10th percentile and median transit times for a transport of 6.5 Sv are shown in parentheses. The red dashed line marks the ordinate limit for the other two panels. The blue bars highlight the distribution of the longest transit times (between 7100 and 8100 years).

It is possible that these time scales would all be shorter if mesoscale eddies were resolved. Ocean models without assimilated data have upwelling transit times for the Southern Ocean that decrease with increasing model horizontal resolution (*56*, *65*): This is not unexpected since vertical velocities increase in magnitude and decrease in scale with increasing resolution. In contrast, the transit times associated with the quasi-horizontal motion around the gyres are comparable at 1/20° and 1° resolutions (*36*, *37*). The important point is the relative difference between transit times in the abyssal cell versus the upper route and subpolar cell, which we anticipate to be robust to changes in resolution.

The multimillennial time scale found for trajectories in the abyssal cell is comparable to that found in idealized simulations (*66*) and Lagrangian analysis (*67*). Given the magnitude of these transit times, the unavoidable hypothesis of statistical equilibrium, implicit in the periodic repetition of the annual cycle velocity field, is certainly questionable. Nevertheless, Fig. 5 indicates that the abyssal cell is responsible for the very old ages observed in the abyssal North Pacific (*68*).

## Salinity export by the MOC

In addition to the volume transport, the salinity transport by the MOC into the Atlantic, an indicator of the stability of the MOC, can be estimated with Lagrangian analysis. The salinity export by the MOC, $T_S$, is defined as

$$T_S \equiv -\sum_{\text{particles}} T_n S_n(x,y,z,t) \quad (2)$$

where $T_n$ is the volume transport of each particle, $S_n$ is its salinity at a given position and time, $(x, y, z, t)$, and the sum is over all particles. Evaluating $T_S$ at the entry and exit sections, both located at 6°S, enables to estimate the net salinity export by the MOC at that location (or at any other section of choice). The salinity transport by the MOC differs from the total salinity transport: Our definition of the MOC restricts $T_n$ to those particles that have gone either through TL, DP, IT, or 6°S below $\sigma_2$ = 36.6 kg/m$^3$, before crossing 6°S above $\sigma_2$ = 36.6 kg/m$^3$. Thus, the salinity transport associated with the shallow locally wind-driven gyres in the South Atlantic is excluded from the Lagrangian estimate in Eq. 2. Excluding the transport by these shallow features is difficult using Eulerian data. Previous observational estimates focusing on the salinity transport by the MOC have made the approximation

$$T_S \approx -\int_{-H}^{0} V^* \bar{S}\, dz \quad (3)$$

where the overbar represents zonal average, and $V^*$ is the zonally integrated baroclinic meridional velocity, i.e., the component with zero vertical integral (*30*, *32*, *33*). The approximation Eq. 3 neglects the correlations arising from the zonal fluctuations in the MOC velocity and salinity. The Lagrangian approach of Eq. 2 provides an unambiguous estimate of the MOC velocities, which includes the correlations of salinity with velocity that is neglected in Eq. 3. These correlations are important because the deep southward branch of the MOC is confined to the western boundary of the South Atlantic,

while the northward shallow return occurs on the eastern side of the basin at 30°S (cf. Fig. 2).

After 8100 years, a fraction of particles in the abyssal cell group has not yet crossed the NADW entry section. Thus, to account for these "slow" particles, we multiply the component of the salinity export due to the abyssal cell by the coefficient of 1.33. This procedure assumes that the salinity-velocity correlation is the same for the fast and slow particles in the abyssal cell group.

The resulting salinity exports by the MOC are as follows [units are in sverdrup practical salinity unit (PSU)]:

At 6°S: $T_s$(NADW) = 480.63; $T_s$(upper) = −488.97; $T_s$(NADW) + $T_s$(upper) = −8.34.

At 30°S: $T_s$(NADW) = 483.20; $T_s$(upper) = −490.62; $T_s$(NADW) + $T_s$(upper) = −7.42.

At both locations, the salinity export in the lower branch of the MOC is smaller than in the upper branch. The net export is negative, i.e., the MOC imports salinity into the Atlantic. This import is amplified at 6°S relative to 30°S. At 30°S, the salinity export by the MOC of −7.4 Sv PSU corresponds to −0.21 Sv at the reference salinity of 34.5 PSU, which should be compared to the previous estimate by Garzoli *et al.* (*33*), who found a climatological average of −0.16 Sv. Using the Eulerian approximation Eq. 3 in ECCOv4, we find a time-averaged MOC salinity export at 30°S of −5.7 Sv PSU. This Eulerian salinity export corresponds to −0.16 Sv at the reference salinity of 34.5 PSU, in agreement with the estimate in (*33*). Our calculations indicate that both the Lagrangian and Eulerian estimates of salinity export by the MOC are negative, consistent with an active salt-advection feedback and potential instability of the AMOC. In addition, the Eulerian approximation Eq. 3 is a lower bound on the Lagrangian value Eq. 2, but the difference is small.

## DISCUSSION

This study examined the coupling between the mid-depth and abyssal components of the global overturning circulation by quantifying the fraction of NADW returning to the upper limb of the AMOC through the upper route (32%) and the lower route (68%). The Lagrangian analysis shows that about half of the NADW transports goes through the abyssal cell, which samples the abyssal Indo-Pacific before returning to the upper limb of the AMOC. Particles in the abyssal cell spend, on average, 1000 years in the abyssal North Pacific, which is half of their time in the AMOC return flow, likely sequestering tracers at that location. Our estimate of the abyssal cell transport is lower than previous ones, implying that a smaller fraction of NADW is available for abyssal storage of carbon, heat, and other tracers (*7*, *19*).

The current consensus is that the densification of NADW to lower buoyancy classes is primarily affected at the Antarctic margin and is thus strongly controlled by sea ice coverage (*25*). Our results challenge this paradigm and show instead that most of the densification of NADW into abyssal water masses occurs at the northern edge of the ACC, with 9% at most occurring near the Antarctic margin. This result could diminish the role of sea ice in the coupling between NADW and the abyssal circulation. While it is possible that this localization stems from inadequate resolution of processes at the Antarctic margin, the strength of the abyssal circulation is controlled by diapycnal mixing: ECCOv4 optimizes this quantity, together with other parametrized transports, to fit a much larger number of observations than those used in previous estimates.

Our Lagrangian analysis does not address the origins of the abyssal circulation entering the Indo-Pacific. In ECCOv4, the Indo-Pacific abyssal circulation amounts to 14.4 Sv, which is larger than the 6.5 Sv whose origin is coupled to the upper limb of the AMOC. The origin and residence times of the remaining 7.9 Sv need to be studied separately.

The other half of NADW transport returns to the AMOC through shallower pathways that are one order of magnitude faster than the abyssal cell: These are the upper route and the subpolar cell. Particles in the subpolar cell sample abyssal densities (Fig. 2), but not abyssal depths (fig. S2), sharing more similarities in pathways, transit times, and diapycnal transformation statistics with the upper route than with the lower route. The separation into two distinct components of the lower route, one of which avoids the abyssal Indo-Pacific, has not been made before. We also find that upwelling into the intermediate and upper density classes largely occurs north of 33°S: This finding limits the role of Southern Ocean upwelling in the MOC to 33%, aggregating all routes.

We find that the MOC imports salinity into the Atlantic, consistent with the salt-advection feedback and potential instability of the mid-depth AMOC. The Lagrangian estimate is slightly larger in magnitude than the corresponding Eulerian approximation, and the Eulerian approximation from ECCOv4 coincides with a previous estimate based on independent observations. We are thus confident that this result is robust and that the Eulerian approximation is useful. Models used for climate projections often have the opposite sign for this index of AMOC stability. Our contribution from a state estimate could be positive encouragement toward addressing this shortcoming in models.

## SUPPLEMENTARY MATERIALS

Supplementary material for this article is available at http://advances.sciencemag.org/cgi/content/full/7/21/eabf5478/DC1

## REFERENCES AND NOTES


1. H. Stommel, Oceanic warming of western Europe. *Proc. Natl. Acad. Sci. U.S.A.* **76**, 2518–2521 (1979).
2. J. Hsiung, Estimates of global oceanic meridional heat transport. *J. Phys. Oceanogr.* **15**, 1405–1413 (1985).
3. K. E. Trenberth, J. M. Caron, Estimates of meridional atmosphere and ocean heat transports. *J. Climate* **14**, 3433–3443 (2001).
4. L. C. Jackson, R. Kahana, T. Graham, M. A. Ringer, T. Woollings, J. V. Mecking, R. A. Wood, Global and European climate impacts of a slowdown of the AMOC in a high resolution GCM. *Climate Dynam.* **45**, 3299–3316 (2015).
5. G. Forget, D. Ferreira, Global ocean heat transport dominated by heat export from the tropical Pacific. *Nat. Geosci.* **12**, 351–354 (2019).
6. J. Bullister, M. Rhein, C. Mauritzen, Deepwater formation, in *Ocean Circulation and Climate: A 21st Century Perspective*, G. Siedler, S. M. Griffies, J. Gould, J. A. Church, Eds. (Academic Press, 2013), pp. 227–253.
7. R. Lumpkin, K. Speer, Global ocean meridional overturning. *J. Phys. Oceanogr.* **37**, 2550–2562 (2007).
8. G. A. MacGilchrist, A. C. Naveira Garabato, P. J. Brown, L. Jullion, S. Bacon, D. C. E. Bakker, M. Hoppema, M. P. Meredith, S. Torres-Valdés, Reframing the carbon cycle of the subpolar Southern Ocean. *Sci. Adv.* **5**, eaav6410 (2019).
9. R. Farneti, S. M. Downes, S. M. Griffies, S. J. Marsland, E. Behrens, M. Bentsen, D. Bi, A. Biastoch, C. Böning, A. Bozec, V. M. Canuto, E. Chassignet, G. Danabasoglu, S. Danilov, N. Diansky, H. Drange, P. G. Fogli, A. Gusev, R. W. Hallberg, A. Howard, M. Ilicak, T. Jung, M. Kelley, W. G. Large, A. Leboissetier, M. Long, J. Lu, S. Masina, A. Mishra, A. Navarra, A. J. George Nurser, L. Patara, B. L. Samuels, D. Sidorenko, H. Tsujino, P. Uotila, Q. Wang, S. G. Yeager, An assessment of Antarctic Circumpolar Current and Southern Ocean meridional overturning circulation during 1958–2007 in a suite of interannual CORE-II simulations. *Ocean Model.* **93**, 84–120 (2015).
10. A. Gordon, "The role of thermohaline circulation in global climate change" (Technical report, Lamont-Doherty Geological Observatory 1990 and 1991 report, Lamont-Doherty Geological Observatory of Columbia University, 1991), pp. 44–51.
11. W. S. Broecker, The great ocean conveyor. *Oceanography* **4**, 79–89 (1991).

12. J. R. Toggweiler, B. Samuels, Effect of Drake Passage on the global thermohaline circulation. *Deep Sea Res. I* **42**, 477–500 (1995).
13. A. L. Gordon, Interocean exchange of thermocline water. *J. Geophys. Res.* **91**, 5037–5046 (1986).
14. P. Cessi, C. Jones, Warm-route versus cold-route interbasin exchange in the meridional overturning circulation. *J. Phys. Oceanogr.* **47**, 1981–1997 (2017).
15. R. Ferrari, L.-P. Nadeau, D. P. Marshall, L. C. Allison, H. L. Johnson, A model of the ocean overturning circulation with two closed basins and a reentrant channel. *J. Phys. Oceanogr.* **47**, 2887–2906 (2017).
16. L.-P. Nadeau, M. F. Jansen, Overturning circulation pathways in a two-basin ocean model. *J. Phys. Oceanogr.* **50**, 2105–2122 (2020).
17. C. L. Wolfe, P. Cessi, The adiabatic pole-to-pole overturning circulation. *J. Phys. Oceanogr.* **41**, 1795–1810 (2011).
18. J. Marshall, K. Speer, Closure of the meridional overturning circulation through Southern Ocean upwelling. *Nat. Geosci.* **5**, 171–180 (2012).
19. L. D. Talley, Closure of the global overturning circulation through the Indian, Pacific, and Southern Oceans: Schematics and transports. *Oceanography* **26**, 80–97 (2013).
20. A. F. Waterhouse, J. A. MacKinnon, J. D. Nash, M. H. Alford, E. Kunze, H. L. Simmons, K. L. Polzin, L. C. St. Laurent, O. M. Sun, R. Pinkel, L. D. Talley, C. B. Whalen, T. N. Huussen, G. S. Carter, I. Fer, S. Waterman, A. C. Naveira Garabato, T. B. Sanford, C. M. Lee, Global patterns of diapycnal mixing from measurements of the turbulent dissipation rate. *J. Phys. Oceanogr.* **44**, 1854–1872 (2014).
21. E. Kunze, The internal-wave-driven meridional overturning circulation. *J. Phys. Oceanogr.* **47**, 2673–2689 (2017).
22. A. Marzocchi, M. F. Jansen, Global cooling linked to increased glacial carbon storage via changes in Antarctic sea ice. *Nat. Geosci.* **12**, 1001–1005 (2019).
23. F. Knox, M. B. McElroy, Changes in atmospheric $CO_2$: Influence of the marine biota at high latitude. *J. Geophys. Res.* **89**, 4629–4637 (1984).
24. J. L. Sarmiento, J. R. Toggweiler, A new model for the role of the oceans in determining atmospheric $P\,CO_2$. *Nature* **308**, 621–624 (1984).
25. R. Ferrari, M. F. Jansen, J. F. Adkins, A. Burke, A. L. Stewart, A. F. Thompson, Antarctic sea ice control on ocean circulation in present and glacial climates. *Proc. Natl. Acad. Sci. U.S.A.* **111**, 8753–8758 (2014).
26. P. Cessi, The global overturning circulation. *Ann. Rev. Mar. Sci.* **11**, 249–270 (2019).
27. S. Rahmstorf, On the freshwater forcing and transport of the Atlantic thermohaline circulation. *Climate Dynam.* **12**, 799–811 (1996).
28. P. de Vries, S. L. Weber, The Atlantic freshwater budget as a diagnostic for the existence of a stable shut down of the meridional overturning circulation. *Geophys. Res. Lett.* **32**, L09606 (2005).
29. H. A. Dijkstra, Characterization of the multiple equilibria regime in a global ocean model. *Tellus* **59A**, 695–705 (2007).
30. S. S. Drijfhout, S. L. Weber, E. van der Swaluw, The stability of the MOC as diagnosed from model projections for pre-industrial, present and future climates. *Climate Dynam.* **37**, 1575–1586 (2011).
31. H. Stommel, Thermohaline convection with two stable regimes of flow. *Tellus* **13**, 224–230 (1961).
32. J. V. Mecking, S. S. Drijfhout, L. C. Jackson, T. Graham, Stable AMOC off state in an eddy-permitting coupled climate model. *Climate Dynam.* **47**, 2455–2470 (2016).
33. S. L. Garzoli, M. O. Baringer, S. Dong, R. C. Perez, Q. Yao, South Atlantic meridional fluxes. *Deep Sea Res. Part I* **71**, 21–32 (2013).
34. K. Döös, Interocean exchange of water masses. *J. Geophys. Res.* **100**, 13499–13514 (1995).
35. S. Speich, B. Blanke, G. Madec, Warm and cold water routes of an O.G.C.M. thermohaline conveyor belt. *Geophys. Res. Lett.* **28**, 311–314 (2001).
36. S. Rühs, F. U. Schwarzkopf, S. Speich, A. Biastoch, Cold vs. warm water route – sources for the upper limb of the Atlantic Meridional Overturning Circulation revisited in a high-resolution ocean model. *Ocean Sci.* **15**, 489–512 (2019).
37. L. Rousselet, P. Cessi, G. Forget, Routes of the upper branch of the Atlantic Meridional Overturning Circulation according to an ocean state estimate. *Geophys. Res. Lett.* **47**, e2020GL089137 (2020).
38. G. Forget, J.-M. Campin, P. Heimbach, C. N. Hill, R. M. Ponte, C. Wunsch, ECCO version 4: An integrated framework for non-linear inverse modeling and global ocean state estimation. *Geosci. Model Dev.* **8**, 3071–3104 (2015).
39. I. Fukumori, O. Wang, I. Fenty, G. Forget, P. Heimbach, R. M. Ponte, "ECCO version 4 release 3" (Technical report, 2017).
40. P. R. Gent, J. C. McWilliams, Isopycnal mixing in ocean circulation models. *J. Phys. Oceanogr.* **20**, 150–155 (1990).
41. M. H. Redi, Oceanic isopycnal mixing by coordinate rotation. *J. Phys. Oceanogr.* **12**, 1154–1158 (1982).
42. G. Forget, D. Ferreira, X. Liang, On the observability of turbulent transport rates by Argo: Supporting evidence from an inversion experiment. *Ocean Sci.* **11**, 839–853 (2015).
43. G. Forget, R. M. Ponte, The partition of regional sea level variability. *Prog. Oceanogr.* **137**, 173–195 (2015).
44. L. C. Jackson, C. Dubois, G. Forget, K. Haines, M. Harrison, D. Iovino, A. Köhl, D. Mignac, S. Masina, K. A. Peterson, C. G. Piecuch, C. D. Roberts, J. Robson, A. Storto, T. Toyoda, M. Valdivieso, C. Wilson, Y. Wang, H. Zuo, The mean state and variability of the north atlantic circulation: A perspective from ocean reanalyses. *J. Geophys. Res. Oceans* **124**, 9141–9170 (2019).
45. S. Cunningham, S. Alderson, B. King, M. Brandon, Transport and variability of the Antarctic Circumpolar Current in Drake Passage. *J. Geophys. Res. Oceans* **108**, 8084 (2003).
46. K. A. Donohue, K. L. Tracey, D. R. Watts, M. P. Chidichimo, T. K. Chereskin, Mean Antarctic circumpolar current transport measured in Drake Passage. *Geophys. Res. Let.* **43**, 11760–11767 (2016).
47. P. Uotila, H. Goosse, K. Haines, M. Chevallier, A. Barthélemy, C. Bricaud, J. Carton, N. Fučkar, G. Garric, D. Iovino, F. Kauker, M. Korhonen, V. S. Lien, M. Marnela, F. Massonnet, D. Mignac, K. A. Peterson, R. Sadikni, L. Shi, S. Tietsche, T. Toyoda, J. Xie, Z. Zhang, An assessment of ten ocean reanalyses in the polar regions. *Climate Dynam.* **52**, 1613–1650 (2019).
48. M. R. Mazloff, P. Heimbach, C. Wunsch, An eddy-permitting Southern Ocean state estimate. *J. Phys. Oceanogr.* **40**, 880–899 (2010).
49. L. D. Talley, Freshwater transport estimates and the global overturning circulation: Shallow, deep, and throughflow components. *Prog. Oceanogr.* **78**, 257–303 (2008).
50. W. R. Young, An exact thickness-weighted average formulation of the Boussinesq equations. *J. Phys. Oceanogr.* **42**, 692–707 (2012).
51. S. M. Griffies, The Gent-McWilliams skew flux. *J. Phys. Oceanogr.* **28**, 831–841 (1998).
52. D. Iudicone, G. Lacorata, V. Rupolo, R. Santoleri, A. Vulpiani, Sensitivity of numerical tracer trajectories to uncertainties in OGCM velocity fields. *Ocean Model.* **4**, 313–325 (2002).
53. X. Qin, E. van Sebille, A. S. Gupta, Quantification of errors induced by temporal resolution on Lagrangian particles in an eddy-resolving model. *Ocean Model.* **76**, 20–30 (2014).
54. B. Blanke, S. Raynaud, Kinematics of the Pacific equatorial undercurrent: An Eulerian and Lagrangian approach from GCM results. *J. Phys. Oceanogr.* **27**, 1038–1053 (1997).
55. S. Speich, B. Blanke, W. Cai, Atlantic meridional overturning circulation and the southern hemisphere supergyre. *Geophys. Res. Lett.* **34**, L23614 (2007).
56. V. Tamsitt, H. F. Drake, A. K. Morrison, L. D. Talley, C. O. Dufour, A. R. Gray, S. M. Griffies, M. R. Mazloff, J. L. Sarmiento, J. Wang, W. Weijer, Spiraling pathways of global deep waters to the surface of the Southern Ocean. *Nat. Commun.* **8**, 172 (2017).
57. S. L. Garzoli, S. Dong, R. Fine, C. S. Meinen, R. C. Perez, C. Schmid, E. van Sebille, Q. Yao, The fate of the deep western boundary current in the South Atlantic. *Deep Sea Res. I Oceanogr. Res. Pap.* **103**, 125–136 (2015).
58. S. M. Chiswell, H. C. Bostock, P. J. Sutton, M. J. Williams, Physical oceanography of the deep seas around New Zealand: A review. *N. Z. J. Mar. Freshw. Res.* **49**, 286–317 (2015).
59. T. Whitworth III, B. A. Warren, W. D. Nowlin, S. B. Rutz, R. D. Pillsbury, M. I. Moore, On the deep western-boundary current in the southwest pacific basin. *Prog. Oceanogr.* **43**, 1–54 (1999).
60. C. de Lavergne, G. Madec, J. Le Sommer, A. J. G. Nurser, A. N. Garabato, On the consumption of Antarctic Bottom Water in the abyssal ocean. *J. Phys. Oceanogr.* **46**, 635–661 (2016).
61. R. Ferrari, A. Mashayek, T. J. McDougall, M. Nikurashin, J.-M. Campin, Turning ocean mixing upside down. *J. Phys. Oceanogr.* **46**, 2239–2261 (2016).
62. T. J. McDougall, R. Ferrari, Abyssal upwelling and downwelling driven by near-boundary mixing. *J. Phys. Oceanogr.* **47**, 261–283 (2017).
63. R. M. Holmes, C. de Lavergne, T. J. McDougall, Ridges, seamounts, troughs and bowls: Topographic control of the dianeutral circulation in the abyssal ocean. *J. Phys. Oceanogr.* **48**, 861–882 (2018).
64. G. MacGilchrist, "Lagrangian perspectives on ocean ventilation," thesis, University of Oxford, Oxford (2017).
65. H. F. Drake, A. K. Morrison, S. M. Griffies, J. L. Sarmiento, W. Weijer, A. R. Gray, Lagrangian timescales of southern ocean upwelling in a hierarchy of model resolutions. *Geophys. Res. Lett.* **45**, 891–898 (2018).
66. M. F. Jansen, L.-P. Nadeau, T. M. Merlis, Transient versus equilibrium response of the ocean's overturning circulation to warming. *J. Climate* **31**, 5147–5163 (2018).
67. S. H. Ali Muttaqi Shah, F. W. Primeau, E. Deleersnijder, A. W. Heemink, Tracing the ventilation pathways of the deep North Pacific Ocean using Lagrangian particles and Eulerian tracers. *J. Phys. Oceanogr.* **47**, 1261–1280 (2017).
68. T. DeVries, F. Primeau, Dynamically and observationally constrained estimates of water-mass distributions and ages in the global ocean. *J. Phys. Oceanogr.* **41**, 2381–2401 (2011).
69. J.-M. Campin, P. Heimbach, M. Losch, G. Forget; edhill3, A. Adcroft; amolod, D. Menemenlis; dfer22, C. Hill, O. Jahn, J. Scott; stephdut, M. Mazloff; baylorfk; antnguyen13, E. Doddridge, I. Fenty, M. Bates, T. Martin, R. Abernathey; samarkhatiwala, T. Smith, J. Lauderdale; hongandyan, B. Deremble, R. Dussin, P. Bourgault; dngoldberg,

A. T. T. McRae, *Mitgcm/mitgcm: checkpoint67m* (2019); https://zenodo.org/record/3492298.
70. G. Forget, *gaelforget/eccov4_flt_offline: Initial public release* (2020); 10.5281/zenodo.4193582.
71. G. Forget, J. TagBot, *Juliaclimate/individualdisplacements.jl* (2020); http://doi.org/10.5281/zenodo.4060606.
72. A. Koch-Larrouy, G. Madec, B. Blanke, R. Molcard, Water mass transformation along the Indonesian throughflow in an OGCM. *Ocean Dynam.* **58**, 289–309 (2008).
73. V. Tamsitt, R. P. Abernathey, M. R. Mazloff, J. Wang, L. D. Talley, Transformation of deep water masses along Lagrangian upwelling pathways in the Southern Ocean. *J. Geophys. Res.* **123**, 1994–2017 (2018).
74. D. R. Jackett, T. J. McDougall, Minimal adjustment of hydrographic profiles to achieve static stability. *J. Atmos. Oceanic Tech.* **12**, 381–389 (1995).

**Acknowledgments**
**Funding:** Funding was provided by the NSF (OCE-1634128) and by the National Aeronautics and Space Administration (80NSSC20K0796). Computational resources were provided by the Extreme Science and Engineering Discovery Environment (NSF grant ACI-1548562). **Author contributions:** L.R. and P.C. conceived the study and designed the Lagrangian computations. G.F. implemented necessary code modifications into the main MITgcm repository that allow for Lagrangian simulations on the global ECCOv4 grid. G.F. provided the initial Lagrangian code from which L.R. started and contributed to initialize the Lagrangian computations. L.R. performed the Lagrangian computations, analysis, and diagnostics generating Figs. 2, 4, and 5, figs. S2 to S5, and the animation. P.C. performed the diagnostics generating Figs. 1 and 3 and fig. S1. All authors contributed to the writing and reviewed and approved the manuscript. **Competing interests:** The authors declare that they have no competing interests. **Data and materials availability:** The monthly climatology used in this study is provided by the ECCO Consortium and is freely available online (https://ecco.jpl.nasa.gov/drive/files/Version4/Release3/). The Lagrangian software used to compute the trajectories is available in the GitHub repository of the MITgcm suite (https://github.com/MITgcm/MITgcm/tree/master/pkg/flt). The modifications necessary for the global ECCOv4 grid are at http://doi.org/10.5281/zenodo.4193582 and http://doi.org/10.5281/zenodo.3967889. The customized Lagrangian code developed for this study is at https://github.com/lourousselet/MITgcm_flt_Rousselet2020.

Submitted 10 November 2020
Accepted 31 March 2021
Published 21 May 2021
10.1126/sciadv.abf5478

**Citation:** L. Rousselet, P. Cessi, G. Forget, Coupling of the mid-depth and abyssal components of the global overturning circulation according to a state estimate. *Sci. Adv.* **7**, eabf5478 (2021).